Crystallization of polypropylene near the surface in injection-molded plaques: A comparison of morphology and a numerical analysis

doi: 10.1002/pen.21864

Crystallization of Polypropylene Near the Surface in Injection-molded Plaques: A Comparison of Morphology and a Numerical Analysis

Yutaka Kobayashi[1,2], Yasuhiko Otsuki[1], Hiroaki Kanno[2], Tomoyoshi Sasakawa[2], Yasuhiro Hanamoto[2], Toshitaka Kanai[2,4]

[1]*Research & Development Division, Prime Polymer Company, Limited, 580-30 Nagaura, Sodegaura-City, Chiba 299-0265, Japan*

[2]*Division of Material Sciences, Graduate School of Natural Science & Technology, Kanazawa University, Kakuma-Machi, Kanazawa-City, Ishikawa 920-1192, Japan*

[3]*Analysis Research Laboratories, Mitsui Chemical Analysis & Consulting Service Incorporated, 580-30 Nagaura, Sodegaura-City, Chiba 299-0265, Japan*

[4]*Research & Development Laboratory, Idemitsu Kosan Company, Limited, Anasaki-Kaigan, Ichihara-City, Chiba 299-0193, Japan*

* Corresponding author.

Present address: R&D division, Advanced Composites, Inc., A1062 S Fourth Avenue, Sidney, OH 45365, USA

Tel.: +1-937-492-9180; fax: +1-937-498-0120.

E-mail address: Yutaka.Kobayashi@advcmp.com (Yutaka Kobayashi).

ABSTRACT

Skin morphology formation on injection-molded isotactic polypropylene (PP) was investigated using micro-beam synchrotron wide-angle X-ray diffraction and numerical simulation. The 1-20-μm depth range was characterized with an X-ray beam of 0.273 μm × 0.389 μm in size. From an evaluation of doping nucleating agents (NA) in PP, the NAs did not work at a depth of 1 μm. α-specified NA affected crystallization within a 5-μm depth. β-specified PP showed α-form crystallinity at the 5-20 μm depth. The mesomorphic crystal near the surface showed extremely high orientation. From viscoelastic flow simulation, PP molecules near the surface were oriented in the flow direction by extensional flow in the flow front, but freezing occurred faster than flow-induced crystallization. It was estimated that the delay of crystallization occurred during the transient temperature. The deformation rate did not cause a difference in crystal morphology near the surface, but the cooling rate did.

INTRODUCTION

The properties of injection-molded isotactic polypropylene (PP) are affected by the molding conditions. A great deal of research has been performed on skin-core morphology in an injection-molded specimen [1-3]. The skin morphology is different from that in other locations because moving molten PP is immediately frozen at the cold cavity wall. In our previous work [4,5], the microhardness and shear stress had their minima at the surface in the depth direction of the injection-molded plaques. Possible causes are low crystalllinity and anisotropy of morphology. Because controlling surface hardness is important in industry, we consider the formation mechanism of skin morphology on injection-molded PP using microbeam synchrotron wide-angle X-ray diffraction (WAXD) and numerical simulation.

In this study, we investigated the effects of nucleating agents (NAs) under quenching conditions to observe whether they increase crystallinity at the surface. We also investigated wheather flow-induced crystallization prevails over nucleation by NAs in PP near the surface during injection molding. Nucleation of PP in the quiescent state is explained by the classical nucleation theory, which is the formation of baby nuclei [6]. The acceleration mechanism of NAs on PP is the reduction of the energy barrier to forming critical nuclei by epitaxy on NA [7,8]. Although the crystallization rate

increases with supercooling, the maximum rate is found between the melting temperature and the glass transition temperature [9]. At cooling rates lower than approximately 30 K/s, the α-form crystal prevails over the mesomorphic form crystal, and the mesomorphic form overpowers the α-form above approximately 80 K/s [10]. Previous work suggests low crystallinity at the surface, where the molten PP at 200 °C contacts the steel wall at 20 °C.

In the surface formation process, the hot molten polymer moves into the mold cavity by fountain flow [11]. At the advancing flow front, the melt flows from the middle of the cavity toward the wall and is subjected to extensional deformation. The oriented melt immediately freezes when it contacts the cold wall. As a result of subsequent flow in the filling process, a shear-oriented layer forms inside the frozen layer. The highly oriented molecular structure can be quantified with birefringence. A depth profile of birefringence from the surface to the shear-oriented layer is generally V-shaped showing a local minimum value [12]. Although the skin morphology along the depth direction can be studied using a micro-beam synchrotron X-ray method [13-14], the V-shaped pattern has not been observed to date because the diameter of the beam is greater than 10 μm and the morphology close to the surface is averaged over a wide area. The greatest difference between this study and previous ones is that we utilize a beam of

0.273 μm × 0.389 μm in size for investigating the relationship between molecular orientation and flow-induced crystallization near the surface.

Our purpose in this study was to clarify the skin morphology formation in the 1-20 μm depth region by a WAXD analysis of three types of nucleated PP and by an original 2-D viscoelastic flow simulation program. Birefringence with a polarizing optical microscope (POM) and micro-beam synchrotron WAXD were utilized for evaluating injection-molding-induced morphology. For the numerical analysis, the multi-mode Phan-Thien-Tanner (PTT) model was adopted in modeling the behavior of the flow front. The simulation focused on the condition of molten polymer near the surface: therefore, modeling of crystallization was ignored.

EXPERIMENTAL

Materials and Molding Conditions

The characteristics of PP used in this study were Ziegler-Natta isotactic homopolymer (MFR 30 g/10min for 2.16 kg at 230 °C, pentad fraction 97%) with a molecular weight of Mw 200 kg/mol and Mw/Mn 4.0. the α-specific NA was sodium 2,2'-methylene-bis-(4,6-di-t-butylphenylene)-phosphate (ADEKA Corp., NA-11) [15]. The β-specific NA was N,N'-dicyclohexylnaphthalene-2,6-dicarboxamide (Shin Nihon Rika, NU 100) [16].

PP and 0.1 wt% of NA were mixed by a twin-screw extruder, TEM-30 (Toshiba Machine), with a barrel temperature of 200 °C. Hereafter, the three types of PP are distinguished as non-NAPP, α-NAPP and β-NAPP, respectively.

Rectangular plaques (^{w}70 mm × ^{l}270 mm × ^{t}3mm) were molded by using an injection-molding machine (Toshiba, IS100F-III). The molding conditions were as follows: mold temperature 40 °C, barrel temperature 200 °C, filling time 3 s, holding time 8 s and curing time 20 s. The injection pressure at the filling process was controlled automatically to maintain constant injection velocity. The holding pressure was manually adjusted to 70% of the filling pressure. These setting conditions resulted in 90 mm/s average fluid velocity in the cavity for the rectangular plaque and a PP temperature of 210 °C.

Morphological Characterization

The molded specimens were characterized by two types of experimental techniques: POM and micro-beam synchrotron WAXD. The POM observation was carried out using an Olympus BH-2 with a Berek compensator at room temperature. As shown in Fig. 1, the morphology of the middle position of the plaques was viewed parallel to the flow direction (edge view). The specimens were microtomed in a sledge microtome at

room temperature in the flow direction to a thickness of 30 μm. In the measurement of birefringence, the sample was oriented 45° to the position of extinction.

The WAXD experiment was carried out using synchrotron radiation at the beam line, BL24XU of SPring-8 at the Japan Synchrotron Radiation Research Institute (JASRI). The instrument used a light collection optical system with zone plates and a detector system with image plates (Rigaku R-AXIS). The square-shaped micro-beam had dimensions of 0.273 μm × 0.389 μm and a wavelength of 1.2398 Å (10 keV). The PP specimens were mounted 52.3 mm from the image plate. The studied positions in the molded plaques are shown in Fig. 1. Measurements were performed at room temperature with the micro-beam being along the flow direction (edge view) and at distances of 1, 5, 20, 100, 200, 500, 1000 and 1500 μm from the surface along the normal direction in the specimens. All of the X-ray data was corrected for background scattering (air and instrument) before analysis.

Crystallinity was calculated as a ratio of the integral of intensities diffracted by a crystalline part and the total integral of intensities [17], namely, a relative value related to the maximum crystallinity measured in the part. Although PP showed polymorphism, crystallinity included all crystal forms, α, β and γ. The degree of orientation was calculated by the azimuthal scans (0-360°) of 2D-WAXD for the (110) lattice plane

[18].

Numerical Method

An original 2-D unsteady-flow simulation program of viscoelastic fluid was used. The numerical method was the same as in the previous work [19]. We assumed dimensionless particles in the fluid and tracked their movement and deformation in the non-isothermal transient condition. Fig 2 shows an FEM model with 1365 nodes and 320 elements, in which axial symmetry conditions were set at the core of the flow channel. The boundary conditions were set as follows: i) at the wall, no-slip, constant coefficient of heat transfer and constant moving velocity: ii) at the inflow, parabolic velocity distribution: and iii) at the interface between melt and air, adiabatic. Although the definition of the y-axis in the calculation was set to zero at the center of the flow channel, the final position, where the motion of a particle stopped in the y-direction, was described as the distance from the surface, as shown in Fig. 3.

Although the kinetics of crystallization can be varied by introducing nucleating agents, their effect on the flow analysis was not considered. The aim of this simulation was to clarify the circumstances of crystallization of PP near the surface. The simulation was carried out using simple governing equations, neglecting compressibility, inertia,

gravity and surface tension and using conservation of mass, conservation of momentum and conservation of energy. As in the constitutive equation, a multi-mode PTT model was adopted in modeling the behavior of the flow front [20, 21]. Numerical simulations were carried out for PP with linear viscoelastic characteristics, as shown in Table 1 and Fig. 4. The distribution of relaxation time was set to 6 modes (0.0001 - 10 s) in the PTT model, at which storage and loss moduli in the experiment and in the numerical simulation coincided. The parameters of the PTT model were fixed at $\varepsilon = 0.5$ and $\xi = 0.12$ in this study. For modeling the temperature dependence of the relaxation time, an Arrhenius type of equation and activation energy of 38 kJ/mol were used.

The cooling behavior was non-isothermally calculated, and crystallization and solidification were ignored. The flow history of stress and strain was detected by tracking the particle in the fluid. Thermal properties were a density of 730 kg/m^3, a specific heat of 3.00 J/g·K and a thermal conductivity of 0.15 J/ms·K. The injection molding conditions were modeled as a PP temperature of 210 °C, a mold temperature of 40 °C, an average fluid velocity of 90 mm/s and a coefficient of heat transfer of 3000 W/m^2·K.

RESULTS AND DISCUSSION

Skin Morphology

To focus on skin morphology, we characterized the frozen layer of injection-molded PP using an X-ray beam of 0.273 μm × 0.389 μm in size. The previous studies utilized X-ray diffraction methods with micro-beams of 10 μm in diameter [13] or 200 μm × 200 μm square [14]. The essential difference between the results in the earlier works [13, 14] and those in the present work is spatial resolution of the skin morphology. A disadvantage of the beam size in this experiment was that it was too small to apply the analysis to the heterogeneous structure. Measurements of the micro-beam WAXD were carried out at depths of 1, 5, 20, 100, 200, 500, 1000 and 1500 μm from the surface in the specimens. We mainly treated the limited area from the surface to a depth of 200 μm, because the crystal morphology was heterogeneous in the 200-1500 μm area of the non-NAPP, as shown in Fig. 5.

Fig. 6 shows the 2-D WAXD patterns at 1 and 5 μm from the surface for the three types of PP. The meridional maximum for the intensity distribution of the diffraction spot was observed at the 1-μm position. Although there were few differences among the three samples, the Bragg spacing was different between the non-NAPP and the NAPPs at the 5-μm position. The 1-D WAXD patterns are shown in Fig. 7. The α-form crystal was identified by diffractions of the (110), (040), (130), (111) and (131)+(041) planes.

The β-form crystal was distinguished by the (300) diffraction [13]. In non-NAPP, the α-form crystal overlapped the mesomorphic form crystal at the 20-μm position. When α-specific NA was added into the PP, the transition between crystal forms was found at the 5-μm position. Although β-specific NA generated a β-form crystal at the 100-μm position, the α-form crystal was observed from 5 μm to 20 μm. The results suggest that crystallization in the 5-20 μm area occurred after the melt cooled to below 90 °C, at which temperature, the crystal growth rate of the α-form is faster than that of the β-form [22]. Although both α- and β-specific NAs increased the crystallinity of PP near the surface (Fig. 8), it was shown that NAs do not work at the 1-μm distance from the surface in the injection-molded plaque.

Orientation Near the Surface

Because the 2-D WAXD patterns suggested strong crystal orientation in the flow direction, the azimuthal scans (0-360°) of 2D-WAXD for the (110) lattice plane were carried out, as shown in Fig. 9. Although the orientation of the mesomorphic form crystal is usually ignored, as in our previous study [4], we included the diffraction of the mesomorphic and α-form crystal in the meridional maxima. The intensity distributions of the diffraction spot on β-NAPP were broad compared to the others. It is well known

that the β-specific NA dissolves partially or completely in the PP melt and recrystallizes during cooling [23]. A possible cause is that the dissolved NA reduces the viscosity of the melt during the large extensional deformation in flow front and decreases the molecular orientation of PP. The degree of orientation is shown in Fig. 10. The orientation near the surface of the non-NAPP was decreased at a depth of 20 μm, and then increased by 200 μm. This V-shaped pattern resembles typical behavior of birefringence in an injection-molded specimen [12]. Fig. 11 shows the depth profile of birefringence measured by the POM with the Berek compensator on the non-NAPP. Although the V-shaped pattern of the birefringence coincides with the orientation measured by the WAXD on non-NAPP, α-NAPP and β-NAPP did not show the clear V-shaped pattern in crystal orientation.

From the comparison of Fig. 5 and Fig. 10, the morphological difference with respect to NA is explained. In the case of non NAPP, the typical three layers were observed: i) a frozen layer from the surface to a depth of 20 μm, ii) the shear-oriented layer from 20 μm to 300 μm, and iii) the core layer, where the orientation of the (110) diffraction was not measured, from 300 μm to the center. For α-NAPP, the crystal orientation was observed from the surface to the center, because the rod-like shape of α-NA caused crystal orientation. The frozen layer was expanded to the 300-μm depth compared to

that of non-NAPP. This indicates that the crystallization was fast due to the nucleation effect. However, β-NAPP showed different morphology compared to α-NAPP. The crystal orientation to the flow direction was not detected from a depth of 200 μm to the center, although the orientation of the (110) diffraction was from the surface to a depth of 20 μm and that of the (300) was at a depth of 100 μm. Consequently, the degree of orientation is affected by not only the shape, but also the rheological change caused by the crystallization rate. In the next section, whether the flow-induced crystallization prevails over nucleation by NA on PP near the surface in injection molding is discussed.

Crystallization Near the Surface in Injection Molding

Crystallization close to the surface of the injection-molded plaque is discussed using the fountain flow concept [11]. To trace the flow history of PP at a specific position in injection-molded specimens, dimensionless particles in the fluid are assumed. Fig. 12 shows movement in the depth direction and the deformation of particles in the non-isothermal transient condition. The particle, which was located at the distance of 3.2 μm from the surface after the fountain flow, originally started near the center (Fig. 12 (a)). When the initial position was far from the center, the final location was far from the surface. As shown in Fig. 12 (b), the particles were subjected to large deformation

when the flow front contacted the mold surface. The deformation of the particles near the surface was fixed after the melt touched the mold because the melt viscosity immediately increased due to quenching. Although crystallization was ignored in the numerical analysis, the frozen-in orientation of molecular chains was estimated. High orientation near the surface observed by WAXD and the POM was formed by this flow history in the flow front. When molecules are highly oriented in the flow direction during the flow, melt entropy is reduced, thus increasing the crystallization temperature [2]. As a result, the rate of nucleation increases with increased supercooling of the melt. The other factors for skin morphology formation should be considered at the same time. The mesomorphic-form crystal is expected due to the high cooling rates at the surface [10]. The relaxation process of stretched polymer chains takes place below the surface.

Firstly, the deformation of molten PP was estimated using the original 2-D viscoelastic flow analysis program. A large extensional deformation occurs just when the melt contacts the cavity wall, and the deformation immediately freezes. Fig. 13 shows the flow history of moving dimensionless particles finally located at distances of 3.2, 13, 46 and 94 μm from the surface. The rate of deformation of the particles relates to molecular orientation near the surface. The reciprocal of the temperature of the particles shows the cooling situation of PP. Although the rate of deformation decreased with the cooling of

the resin temperature, few differences in the rate were detected with the depth. From the results, the melt entropy for crystallization was almost same at the surface to a depth 100 μm. We considered that the difference in crystallinity along the depth direction was caused by the cooling condition in the injection molding.

As shown in Fig. 14, the cooling rate of the particles was different in the depth direction. The particle at a depth of 22 μm was quenched by 83 °C at a rate of more than 73 °C/s. At a depth of 20 μm in actual specimens, non-NAPP showed α-form crystals and β-specific NA promoted α-form crystals instead of the β-form. Previous studies have suggested that the mesomorphic form prevails over the α-form above approximately 80 °C/s [10], and the crystal growth rate of α-form is faster than that of the β-form crystal when the temperature is lower than 90 °C [22]. The supercooled melt crystallizes after the temperature decreases. The crystallinity stays constant inside the 100-μm depth because the crystallization temperature is expected to be higher than 123 °C. Our previous study suggested that the frozen-in orientation near the surface occurred at high temperature [19]. High orientation near the surface was also observed in this study, even if the crystallinity was low. Accordingly, stretched PP chains cannot move into a specific space layout as a monoclinic unit cell. A high-order structure akin to a shish-kebab does not form near the surface, but mesomorphic form crystals exist

there. Crystallization should be considered separate from frozen-in orientation.

The overall crystallization mechanism of PP near the surface in injection molding is summarized as follows: (a) Molten PP is extensionally stretched at the flow front: (b) after contacting the cold wall, the melt is quenched, but crystallization is delayed during transient temperature, and (c) the crystallinity near the surface depends on the temperature at depth.

CONCLUSION

The skin morphology formation of PP in injection-molded plaques was investigated using X-ray diffraction and numerical simulation. Using an X-ray beam of 0.273 μm × 0.389 μm in size, the skin morphology from the surface to a 100-μm depth was observed. The degree of orientation measured on mesomorphic and α-form crystals showed a V-shaped pattern with typical birefringence behavior, although the crystallinity constantly decreased from the interior to the surface. In injection molding, NA did not work on the crystallization of PP at the 1-μm depth, and mesomorphic phase was observed. NAs promoted crystallization from a depth of 5 μm to the core. The observed skin morphology was compared to the factors calculated by numerical viscoelastic analysis of fountain flow. The crystallinity was affect not by the

deformation rate of the melt but by the cooling rate and the temperature after quenching.

ACKNOWLEDGMENT

A part of this work was performed at the beam-line BL24XU of SPring-8 at the Japan Synchrotron Radiation Research Institute (JASRI). Prime Polymer Co., Ltd. is acknowledged for permitting the release of this study.

REFERENCES

1. R.A. Phillips and M.D. Wolkowicz, "Polypropylene Morphology" in Polypropylene hand book, 2nd, N. Pasquini, Ed., Carl Hanser Verlag, Munich (2005).

2. R. Pantani, I. Coccorullo, V. Speranza, and G. Titomanlio, *Prog. Polym. Sci.*, **30**, 1185 (2005).

3. J.C. Viana, A.M. Cunha, and N. Billon, *Polymer*, **43**, 4185 (2002).

4. Y. Kobayashi, H. Kanno, Y. Hanamoto, M. Ando, and T. Kanai, *J. Appl. Polym. Sci.*, **116**, 1823 (2010).

5. Y. Kobayashi, M. Ando, and T. Kanai, *J. Appl. Polym. Sci.*, **116**, 2590 (2010).

6. P. Panine, E.D. Cola, M. Sztucki, and T. Narayanan, *Polymer*, **49**, 676 (2008).

7. K. Okada, K. Watanabe, Y. Urushihara, A. Toda, and M. Hikosaka, *Polymer*, **48**, 401 (2007).

8. T. Urushihara, K. Okada, K. Watanabe, A. Toda, N. Kawamoto, and M. Hikosaka, *Polym. J.*, **41**, 228 (2009).

9. N. Okui, S. Umemoto, R. Kawano, and Al Mamun, "Temperature and Molecular Weight Dependencies of Polymer Crystallization" in Progress in Understanding of Polymer Crystallization, G. Reiter, Ed., Springer-Verlag, Berlin (2007).

10. I. Coccorullo, R. Pantani, and G. Titomanlio, *Polymer*, **44**, 307 (2003).

11. Z. Tadmor, *J. Appl. Polym. Sci.*, **18**, 1753 (1974).

12. D. Choi and J.L.White, *Polym. Eng. Sci.*, **42**, 1642 (2002).

13. J.W. Housmans, M. Gahleitner, G.W.M. Peters, and H.E.H. Meijer, *Polymer*, **50**, 230 (2009).

14. P. Zhu and G. Edward, *Polymer*, **45**, 2603 (2004).

15. T. Urushihara, K. Okada, K. Watanabe, A. Tada, E. Tobita, N. Kawamoto, and M. Hikosaka, *Polym. J.*, **39**, 55 (2007).

16 L. Chvátlová, J. Navrátilová, R. Čermák, M. Raab, and M. Obadal, *Macromolecules*, **42**, 7413 (2009).

17. G. Natta, P. Corradini, and M. Cesari, *Atti della Accademia nazionale dei Lincei, Rendiconti*, **22**, 11 (1957).

18. M. Kakudo and N. Kasai, *X-ray Diffraction by Polymers*, Kodansha, Tokyo (1972).

19. Y. Kobayashi, Y. Otsuki, and T. Kanai, *Polym. Eng. Sci.*, in press.

20. N. Phan-Thien and R.I.Tanner, *J. Non-Newtonian Fluid Mech.*, **2**, 353 (1977).

21. N. Phan-Thien, *J. Non-Newtonian Fluid Mech.*, **26**, 327 (1988).

22. K. Nakamura, S. Shimizu, S. Umemoto, A. Thierry, B. Lotz, and N. Okui, *Polym. J.*, **40**, 915 (2008).

23. J. Varga and A. Menyhárd, *Macromolecules*, **40**, 2422 (2007).

Table 1. A distribution of relaxation time and modulus of PP.

Relaxation time (s)	Relaxation modulus (Pa)
10	1.5
1	120
0.1	2600
0.01	18000
0.001	60000
0.0001	100000

FIGURE CAPTIONS

FIG. 1. A schematic diagram of an injection-molded plaque and specimen cut at the central position.

FIG. 2. Schematic diagrams of the FEM model used in the numerical simulation. (a) A static state; 1365 node number and 320 elements, in which axial symmetry conditions are set at the center of the flow channel. (b) Steady-state boundary conditions; an average fluid velocity of 90 mm/s, a resin temperature of 210 °C, a mold temperature of 40 °C and a coefficient of heat transfer of 3000 $w/m^2 \cdot K$.

FIG. 3. A conceptual diagram for particle motion in the flow front. A particle starting at the initial position is subject to large deformation and moves to the final position.

FIG. 4. Plot of storage (G') and loss (G") moduli experimentally measured and numerically calculated with six mode relaxation times for the PTT model. The horizontal axis indicates angular frequency at 210 °C. G' and G" for a single relaxation time are shown by the thick and thin dashed lines, respectively.

FIG. 5. Morphology of the cross-cut section observed by a POM. Micrograph along the flow direction with the specimen rotated by 45° from the direction of the polarizer: (a) non-NAPP, (b) α-NAPP and (c) β-NAPP.

FIG. 6. Two-dimensional WAXD patterns at 1 and 5 μm from the surface for

injection-molded PP: (a) non-NAPP, (b) α-NAPP and (c) β-NAPP. These images represent the raw patterns without background correction.

FIG. 7. Changes in X-ray diffraction patterns in the depth direction. Distances from the surface are 1, 20 and 100 μm: (a) non-NAPP, (b) α-NAPP and (c) β-NAPP.

FIG. 8. Changes in crystallinity from the surface to the core in injection-molded specimens. Conditions: edge view, beam dimensions 0.273 μm × 0.389 μm, room temperature.

FIG. 9. Changes in 110 azimuthal intensity in the depth direction. Distances from surface are 1 and 5 μm: (a) non-NAPP, (b) α-NAPP and (c) β-NAPP.

FIG. 10. Changes in orientation from the surface to the core in injection-molded specimens. Conditions: edge view, beam dimensions 0.273 μm × 0.389 μm, room temperature.

FIG. 11. Changes in birefringence on non-NAPP along the depth direction.

FIG. 12. Flow history of particles, which had final locations at the depths 3.2, 22, 46 and 94 μm. (a) Changes in position of particles along the depth direction over time. (b) Changes in first invariant of Finger strain tensor over time.

FIG. 13. The relationship between the rate of deformation and resin temperature at different depths, calculated by the original 2-D viscoelastic flow simulation program.

FIG. 14. The relationship between the cooling rate and resin temperature at different depths, calculated by the original 2-D viscoelastic flow simulation program.

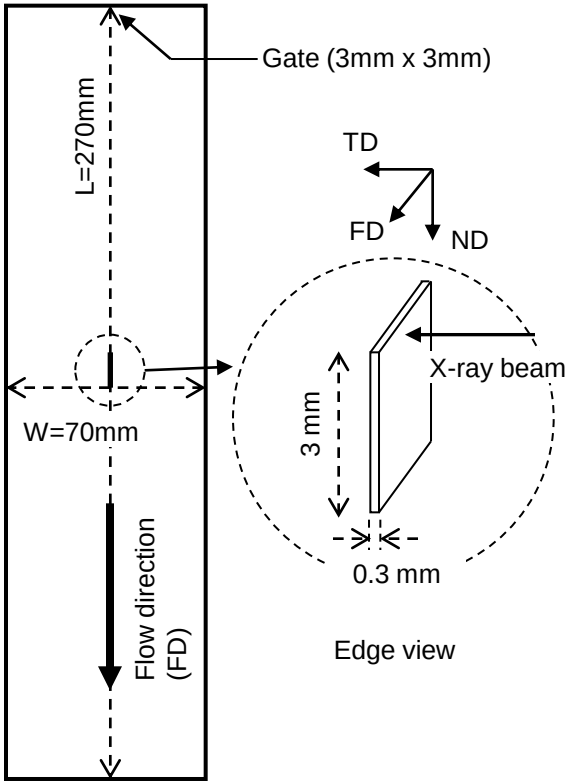

FIG. 1. A schematic diagram of an injection-molded plaque and specimen cut at the central position.

Table 1 A distribution of relaxation time and modulus of PP

Relaxation time (s)	Relaxation modulus (Pa)
10	1.5
1	120
0.1	2600
0.01	18000
0.001	60000
0.0001	100000

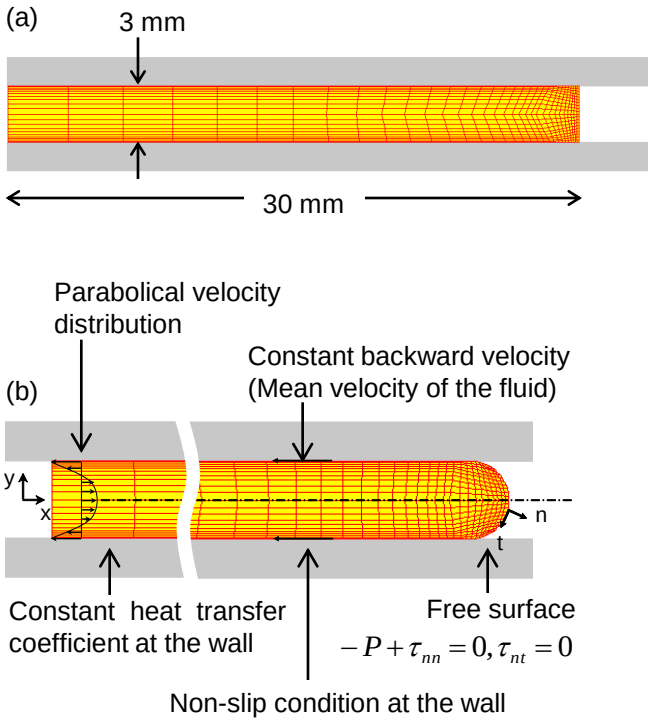

FIG. 2. Schematic diagrams of the FEM model used in the numerical simulation. (a) A static state; 1365 node number and 320 elements. (b) Steady-state boundary conditions; an average fluid velocity of 90 mm/s, a resin temperature of 210 °C, a mold temperature of 40 °C and a coefficient of heat transfer of 3000 w/m^2·K.

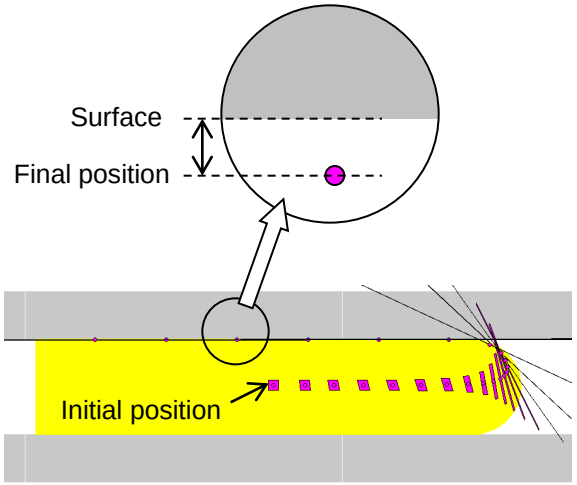

FIG. 3. A conceptual diagram for particle motion in the flow front. A particle starting at the initial position is subject to large deformation and moves to the final position.

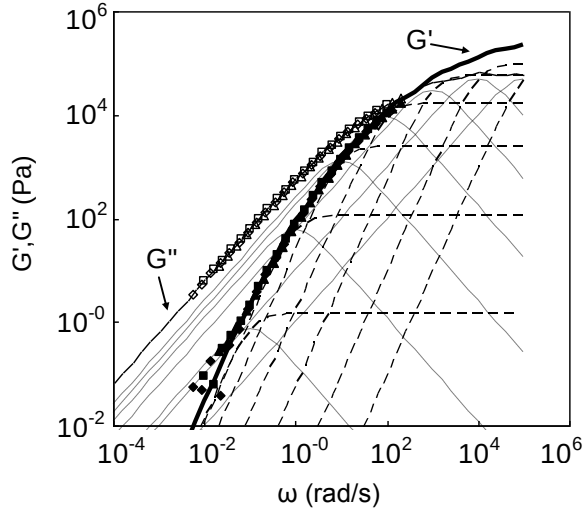

FIG. 4. Plot of storage (G') and loss (G") moduli experimentally measured and numerically calculated with six mode relaxation times for the PTT model. The horizontal axis indicates angular frequency at 210 °C. G' and G" for a single relaxation time are shown by the thick and thin dashed lines, respectively.

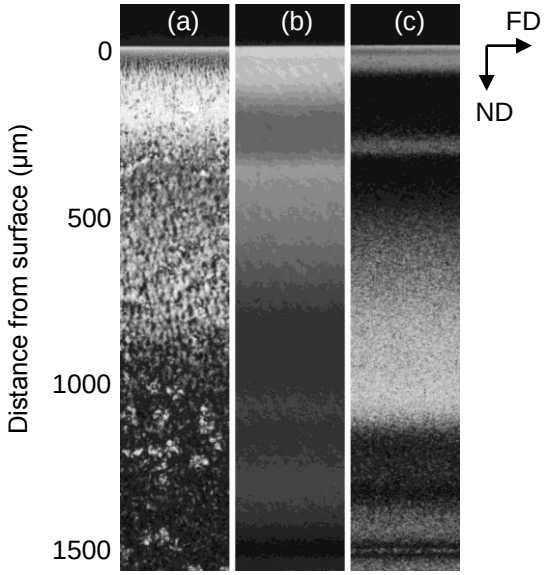

FIG. 5. Morphology of the cross-cut section observed by a POM. Micrograph along the flow direction with the specimen rotated by 45° from the direction of the polarizer: (a) non-NAPP, (b) α-NAPP and (c) β-NAPP.

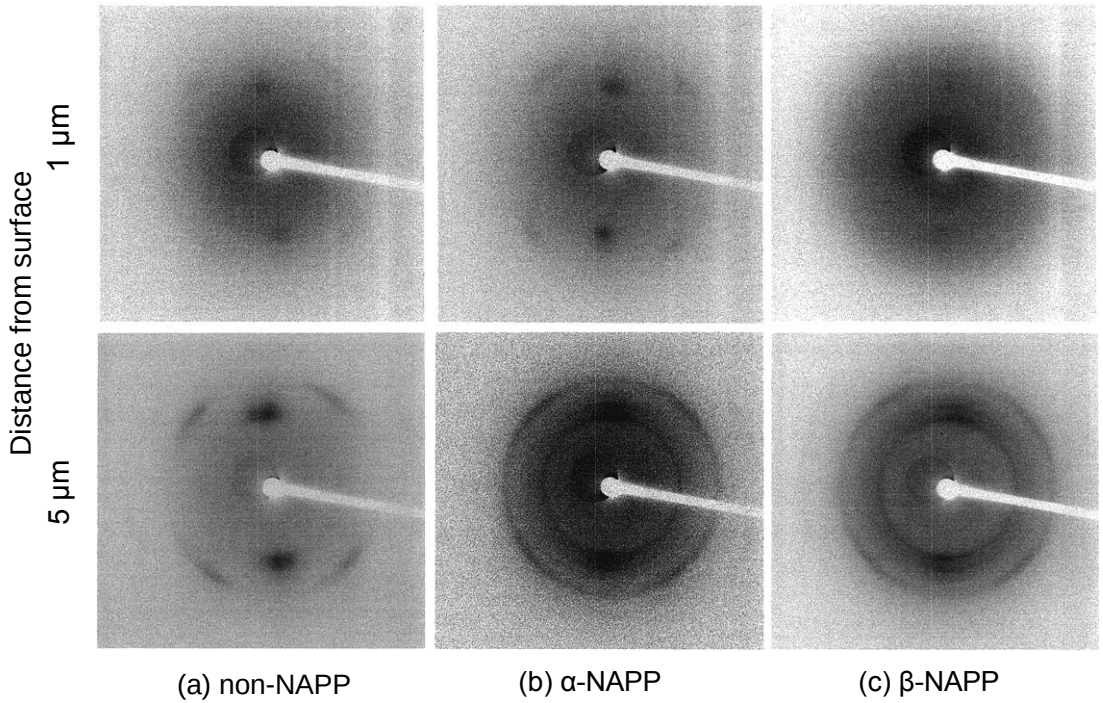

FIG. 6. Two-dimensional WAXD patterns at 1 and 5 μm from the surface for injection-molded PP: (a) non-NAPP, (b) α-NAPP and (c) β-NAPP. These images represent the raw patterns without background correction.

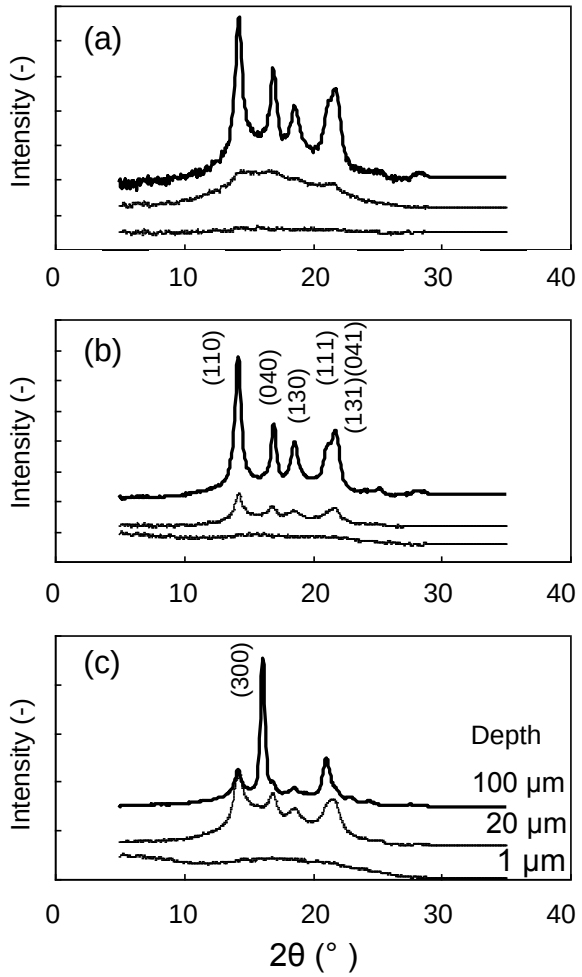

FIG. 7. Changes in X-ray diffraction patterns in the depth direction. Distances from the surface are 1, 20 and 100 μm: (a) non-NAPP, (b) α-NAPP and (c) β-NAPP.

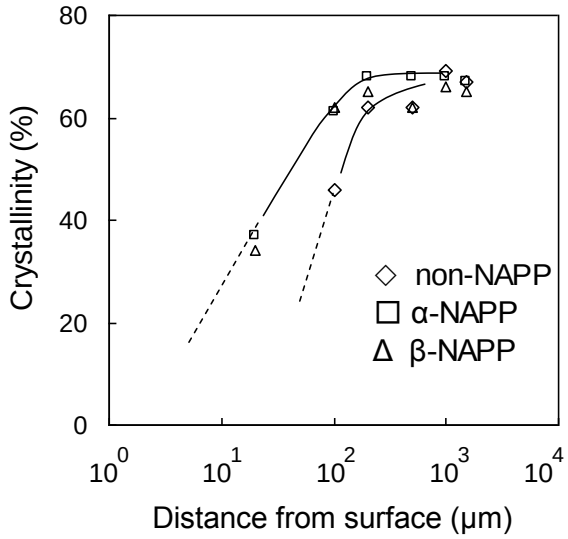

FIG. 8. Changes in crystallinity from the surface to the core in injection-molded specimens. Conditions: edge view, beam dimensions 0.273 μm × 0.389 μm, room temperature.

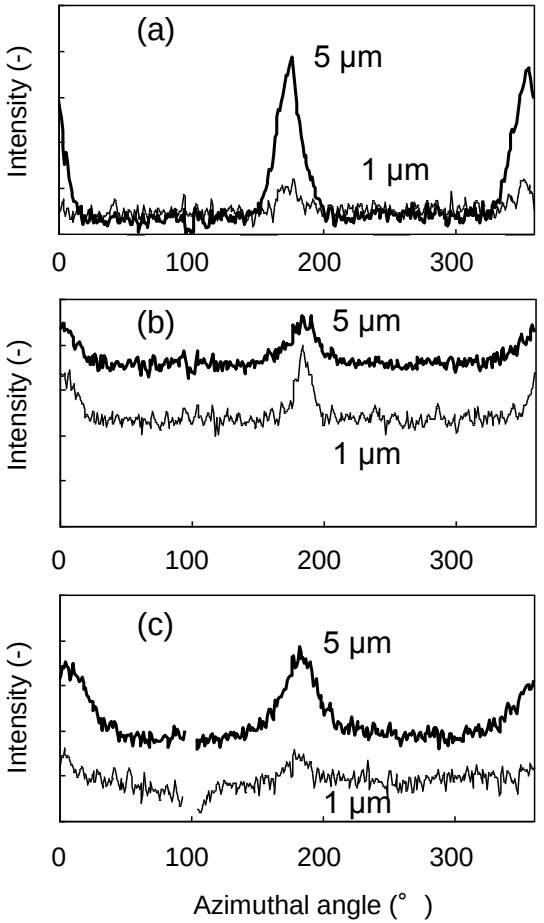

FIG. 9. Changes in 110 azimuthal intensity in the depth direction. Distances from surface are 1 and 5 μm: (a) non-NAPP, (b) α-NAPP and (c) β-NAPP.

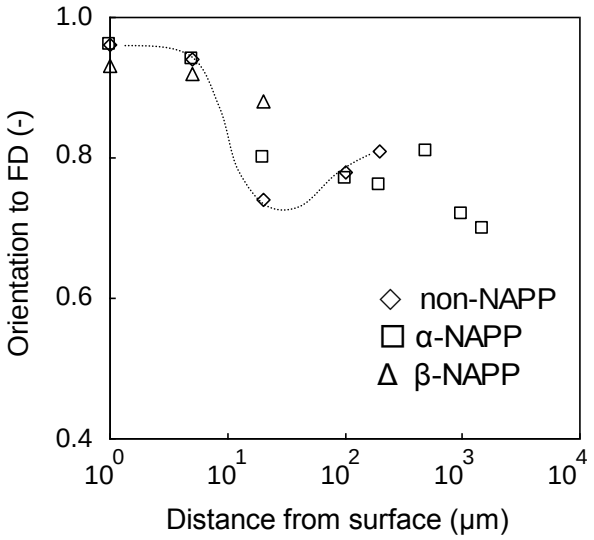

FIG. 10. Changes in orientation from the surface to the core in injection-molded specimens. Conditions: edge view, beam dimensions 0.273 μm × 0.389 μm, room temperature.

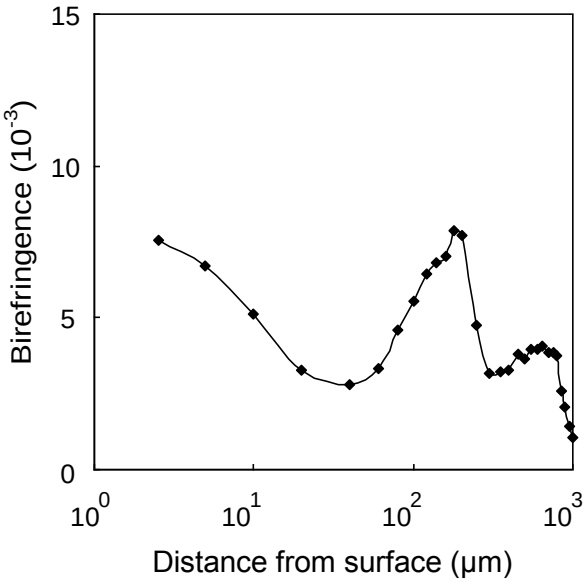

FIG. 11. Changes in birefringence on non-NAPP along the depth direction.

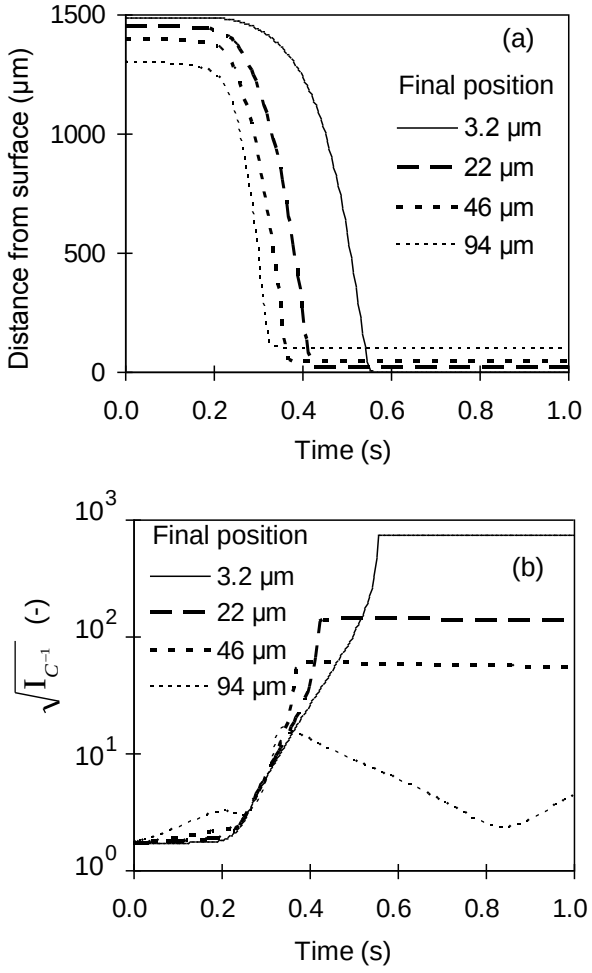

FIG. 12. Flow history of particles, which had final locations at the depths 3.2, 22, 46 and 94 μm. (a) Changes in position of particles along the depth direction over time. (b) Changes in first invariant of Finger strain tensor over time.

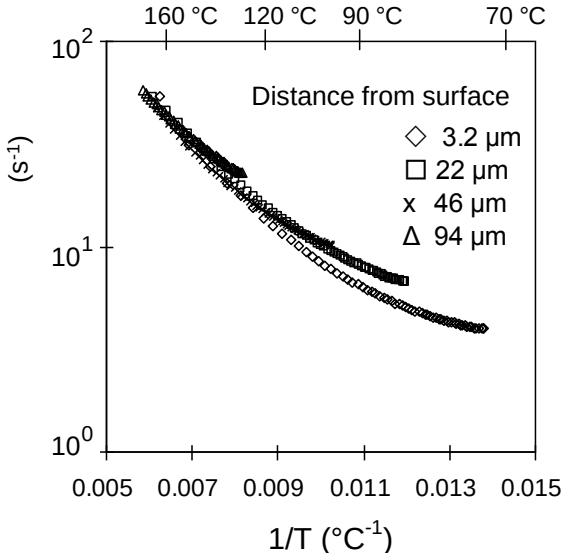

FIG. 13. The relationship between the rate of deformation and resin temperature at different depths, calculated by the original 2-D viscoelastic flow simulation program.

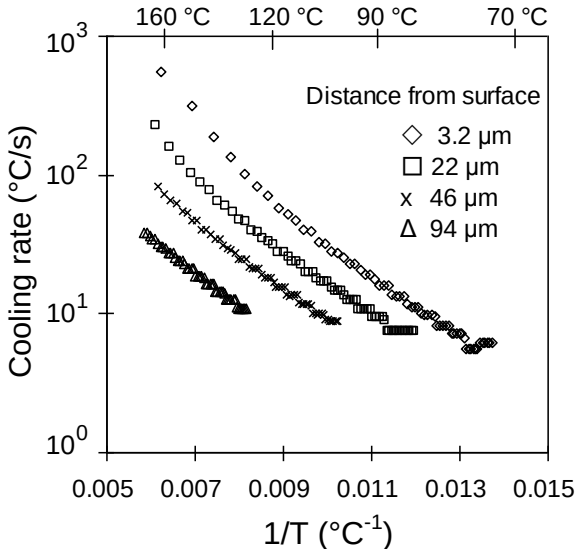

FIG. 14. The relationship between the cooling rate and resin temperature at different depths, calculated by the original 2-D viscoelastic flow simulation program.